

Jet Substructure Without Trees

MARTIN JANKOWIAK¹ AND ANDREW J. LARKOSKI²*SLAC, Menlo Park, CA 94025*
SITP, Stanford University, Stanford, CA 94305

ABSTRACT

We present an alternative approach to identifying and characterizing jet substructure. An angular correlation function is introduced that can be used to extract angular and mass scales within a jet without reference to a clustering algorithm. This procedure gives rise to a number of useful jet observables. As an application, we construct a top quark tagging algorithm that is competitive with existing methods.

¹janko@stanford.edu²larkoski@stanford.edu

1 Introduction

In preparation for the LHC, the past several years have seen extensive work on various aspects of collider searches. With the excellent resolution of the ATLAS and CMS detectors as a catalyst, one area that has undergone significant development is jet substructure physics. The use of jet substructure techniques, which probe the fine-grained details of how energy is distributed in jets, has two broad goals. First, measuring more than just the bulk properties of jets allows for additional probes of QCD. For example, jet substructure measurements can be compared against precision perturbative QCD calculations or used to tune Monte Carlo event generators. Second, jet substructure allows for additional handles in event discrimination. These handles could play an important role at the LHC in discriminating between signal and background events in a wide variety of particle searches. For example, Monte Carlo studies indicate that jet substructure techniques allow for efficient reconstruction of boosted heavy objects such as the W^\pm and Z^0 gauge bosons [1–4], the top quark [5–10], and the Higgs boson [11–16].

At least two broad classes of jet substructure techniques have been developed. The first class employs jet shape observables to probe energy distribution in jets. The second class makes use of the clustering tree of a jet as constructed by the Cambridge-Aachen (CA) [17] or k_T [18] sequential jet clustering algorithms to identify and characterize subjets within the jet.

Jet shape observables offer a measure of how energy is distributed within a jet. The energy distribution of a jet is determined by a variety of factors, including heavy particle decays, color flow, and the dynamics of the parton shower. Different jet shape observables have been constructed to quantify these [19–24] and other aspects of jet substructure. Infrared and collinear (IRC) safe observables can in principle be computed in perturbation theory or modeled with Monte Carlo simulations and then compared to experimental results. Combining different jet shape observables has been shown to provide for effective discrimination in a variety of different scenarios (see e.g. [25]). A disadvantage of jet shape observables is that, because they can only be computed once the constituents of the jet have been defined, they cannot be used to determine how to most effectively select jets within a given event. In particular a jet shape observable is only as good as the choice of particles that define the jet. As a result jet shape observables do not offer a way of selectively removing likely contamination from underlying event or pile-up[†].

The CA and k_T sequential jet algorithms are defined by metrics d_{ij} that have been chosen with the goal of constructing clustering trees that closely approximate the perturbative QCD parton shower. The first few branches of the clustering tree can

[†]See however [26]

be used to decompose a jet into subjets. This unclustering procedure has seen a wide variety of phenomenological applications, especially in the context of tagging jets that result from boosted heavy particle decays, *e.g.* filtering in boosted Higgs searches [11]. A closely related procedure, referred to as pruning [27], vetoes on QCD-like branches with the goal of sharpening jet mass resolution. This family of procedures offers a number of tunable parameters, allowing the user to control how much and what kind of substructure is identified. A disadvantage of these procedures is that, in order for them to be most effective, the clustering tree must accurately reconstruct the parton shower history of the jet. In practice the CA and k_T algorithms reconstruct the most probable shower history, which need not coincide with the actual shower history. In addition, the parameters which define the unclustering typically impose a hard line between QCD-like behavior and non-QCD-like behavior that can fail to accommodate jets that deviate too much from “most probable” jets.

The goal of this paper is to explore an alternative procedure for identifying and characterizing substructure within jets. The discussion is organized as follows. In Section 2, we introduce the “angular correlation function” $\mathcal{G}(R)$ and discuss how structure in $\mathcal{G}(R)$ can be used to construct IRC safe jet observables. In particular we use $\mathcal{G}(R)$ to extract angular scales R_* and mass scales m_* directly from the constituents of a jet without use of a clustering tree. These angular and mass scales correspond to the angular separations and invariant masses of pairs of hard substructure in the jet. In Section 3, we present an application of these ideas to the tagging of boosted top quarks. We find that the resulting top tagging algorithm is competitive with other methods in the literature. Given the straightforward approach we take in applying $\mathcal{G}(R)$ to top tagging, this good performance ‘out of the box’ is encouraging. In Section 4 we discuss other possible applications of the methods introduced in this paper.

2 Angular Correlation Function

To characterize substructure in a jet J we define the angular correlation function $\mathcal{G}(R)$ as

$$\mathcal{G}(R) \equiv \frac{\sum_{i \neq j} p_{Ti} p_{Tj} \Delta R_{ij}^2 \Theta(R - \Delta R_{ij})}{\sum_{i \neq j} p_{Ti} p_{Tj} \Delta R_{ij}^2} \approx \frac{\sum_{i \neq j} p_i \cdot p_j \Theta(R - \Delta R_{ij})}{\sum_{i \neq j} p_i \cdot p_j} \quad (1)$$

where the sum runs over all pairs of constituents of J and $\Theta(x)$ is the Heaviside step function. Here p_{Ti} is the transverse momentum of constituent i , and ΔR_{ij} is the Euclidean distance between i and j in the pseudorapidity (η) and azimuthal angle

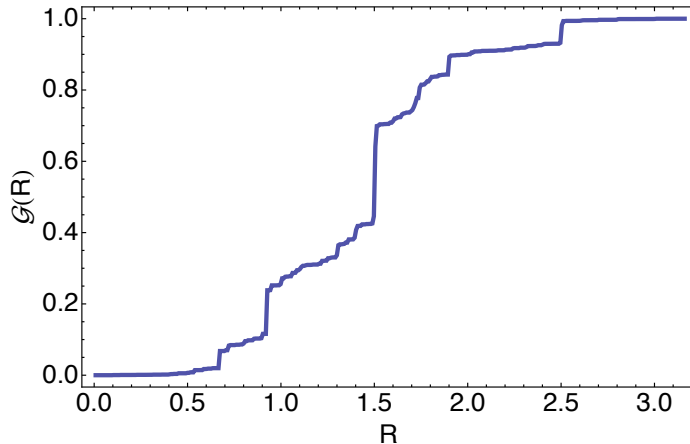


Figure 1: The angular correlation function $\mathcal{G}(R)$ for a sample top jet.

(ϕ) plane: $\Delta R_{ij}^2 = (\eta_i - \eta_j)^2 + (\phi_i - \phi_j)^2$. On the LHS of Eq. (1) the dependence on transverse momenta is fixed by collinear safety. Provided that ΔR_{ij} is raised to a positive power, the entire expression is IRC safe. We choose ΔR_{ij}^2 in Eq. (1) so that $\mathcal{G}(R)$ has a clear physical interpretation: $\mathcal{G}(R)$ is the (fractional) mass contribution from constituents separated by an angular distance of R or less. An important point here is that R does *not* mark the distance with respect to any fixed center.

For a jet with no substructure, $\mathcal{G}(R)$ is featureless. In contrast, if a jet has significant substructure at an angular scale $R = R_*$, $\mathcal{G}(R)$ exhibits a discontinuous ledge at $R = R_*$, see Fig. 1. Such a ledge corresponds to two or more hard subjets separated by a distance R_* from one another, with the ledge drop determined by the invariant mass of the subjets. Notice that these ledges are closely related to mass drops as exploited in a variety of jet substructure studies [8–12]. We expect that a typical QCD jet will have an angular correlation function that is more or less smoothly varying without any sharp ledges, while for a jet with significant substructure $\mathcal{G}(R)$ will have one or more sharp ledges at angular scales $R = R_*$ corresponding to distinct separations between hard subjets in the jet. This suggests several jet observables that can be defined from $\mathcal{G}(R)$. Given a procedure for finding ledges in $\mathcal{G}(R)$, we can consider: (i) the total number of ledges; (ii) the angular scales $R = R_*$ at which ledges are found; and (iii) the ledge drops at each $R = R_*$. We will see that, once suitably defined, each of the resulting observables proves useful in characterizing substructure within jets.

In effect, $\mathcal{G}(R)$ defines a continuous family of jet shape observables. Each $\mathcal{G}(R_0)$ for a given R_0 differs from most jet shape observables in that: (i) it does not contain any preferred or reference four-vectors (e.g. the energy center of the jet); and (ii) it involves a sum over *two-particle* correlations. For example, the radial jet energy

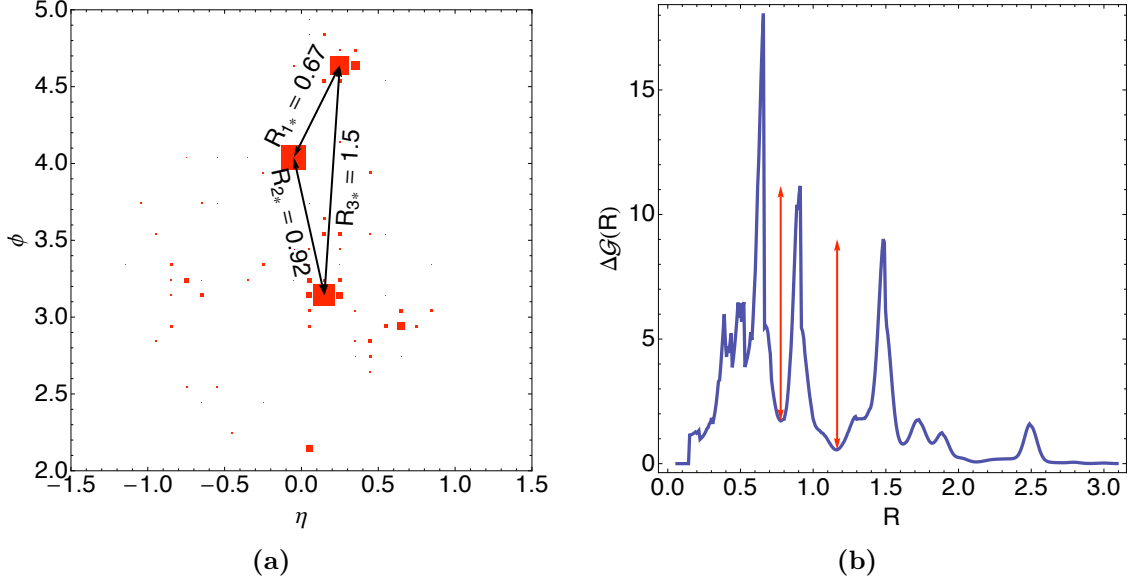


Figure 2: p_T plot and angular structure function $\Delta\mathcal{G}(R)$ for the top jet whose $\mathcal{G}(R)$ is illustrated in Fig. 1. **(a)** The p_T plot depicts the transverse energy deposited in calorimeter cells of size 0.1×0.1 in (η, ϕ) with the area of each red square proportional to the p_T . This top has $p_T \sim 300$ GeV and a clean three-pronged substructure. **(b)** For a minimum prominence of 4.0, $\Delta\mathcal{G}(R)$ has three peaks with $R_{1*} = 0.66$, $R_{2*} = 0.91$, and $R_{3*} = 1.48$. The red arrows illustrate the prominence of the two peaks at R_{2*} and R_{3*} .

profile $\psi(R)$ as in [28, 29] quantifies the fraction of a jet’s energy that is contained within an angular distance R of the center of the jet. Although $\psi(R)$ for a top jet will exhibit discontinuous ledges at particular angular scales, these scales are not useful for characterizing the substructure of the jet. This is because the resulting angular scales, which are defined with respect to the jet center, cannot be used to reconstruct the separations between the three top subjets. In addition, the invariant masses of pairs of subjets are not accessible from $\psi(R)$. The angular correlation function $\mathcal{G}(R)$ is closer in spirit to factorial moments as in [30], which were introduced to quantify scaling behavior in multi-particle production.

In order for the observables derived from $\mathcal{G}(R)$ to be useful, care must be taken in defining them. We find that, instead of directly finding ledges in $\mathcal{G}(R)$, it is preferable to find peaks in a suitably chosen derivative of $\mathcal{G}(R)$. In particular, because we are interested in ratios of mass scales, we should look for structure in $\log \mathcal{G}(R)^\ddagger$. Because QCD is approximately scale invariant, structure in $\log \mathcal{G}(R)$ should be identified by calculating derivatives with respect to $\log R$. Since $d/d\log R = R d/dR$,

[‡] The normalization in $\mathcal{G}(R)$ has been chosen with this logarithm in mind: $\mathcal{G}(R)$ increases monotonically from 0 to 1 as R increases from $R = 0$ to $R = \max \Delta R_{ij}$.

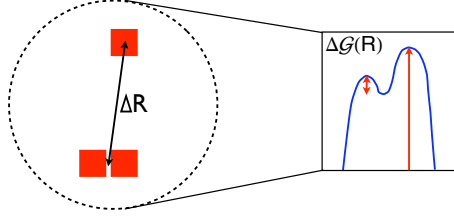


Figure 3: An illustration of how prominence requirements, by selecting peaks that stand out above background noise, prevent angular scales from being double-counted.

this choice ensures that noise in $\log \mathcal{G}(R)$ at small R does not result in extraneous peaks. This suggests that the quantity of interest is $d \log \mathcal{G}(R)/d \log R$. A concern with $d \log \mathcal{G}(R)/d \log R$ is that the derivative produces a delta function $\delta(R - \Delta R_{ij})$; as a consequence, $d \log \mathcal{G}(R)/d \log R$ defines a noisy function of R . Therefore, to identify structure in $\log \mathcal{G}(R)$ we define an “angular structure function” $\Delta \mathcal{G}(R)$ by replacing the delta function in $d \log \mathcal{G}(R)/d \log R$ with a smooth kernel $K(x)$:

$$\Delta \mathcal{G}(R) \equiv R \frac{\sum_{i \neq j} p_{Ti} p_{Tj} \Delta R_{ij}^2 K(R - \Delta R_{ij})}{\sum_{i \neq j} p_{Ti} p_{Tj} \Delta R_{ij}^2 \Theta(R - \Delta R_{ij})} \quad (2)$$

In the following we choose a gaussian $K(x) = e^{-x^2/dR^2}/\sqrt{\pi dR^2}$ with $dR = 0.06$. We find that this choice reduces noise substantially. This value of dR was selected after scanning a range $dR \in [0.02, 0.12]$ and choosing dR to maximize the performance of the top tagging algorithm presented in Sec. 3.

To identify angular scales $R = R_*$ in the jet that correspond to distinct hard substructure in the event, it is important to find peaks in $\Delta \mathcal{G}(R)$ in a way that is robust against noise.[§] For this purpose we borrow a concept from geography called (topographic) prominence [31]. The prominence of the highest peak is defined as its height. In the mountaineering analogy, the prominence of any lower peak P is defined as the minimum vertical descent that is required in descending from P before ascending a higher, neighboring peak P' , where P' can lie to either side of P . Fig. 2(b) illustrates this concept for two different peaks. In Fig. 3 we illustrate how using prominence instead of height to identify physical peaks can eliminate extraneous peaks that are artifacts of the detector’s finite angular resolution. The pictured jet has two distinct hard subjets separated by a single angular scale ΔR . Since one of the subjets has its energy deposited in two neighboring calorimeter cells, the angular structure function $\Delta \mathcal{G}(R)$ exhibits two distinct peaks in the neighborhood of $R = \Delta R$. Only one of the two peaks has a large prominence, and so using prominence to select peaks in $\Delta \mathcal{G}(R)$ ensures that only a single angular scale near $R = \Delta R$ is identified.

[§]Using the kernel $K(x)$ reduces the noise in $\Delta \mathcal{G}(R)$ but does not do so completely.

In the following we will identify a peak in $\Delta\mathcal{G}(R)$ by demanding that its prominence exceeds a minimum value h_0 .

So far we have described how to define two different jet observables from prominent peaks in $\Delta\mathcal{G}(R)$. The first is n_p , the number of prominent peaks in $\Delta\mathcal{G}(R)$. The second is the various angular scales R_{i*} at which prominent peaks are located. It remains to define a jet observable that corresponds to ledge drops in $\mathcal{G}(R)$. The magnitude of a ledge drop in $\mathcal{G}(R)$ will map onto the height of the corresponding peak in $\Delta\mathcal{G}(R)$. This height is determined by the invariant mass of (typically) two hard subjets separated by an angular distance $R = R_{i*}$. For each prominent peak in $\Delta\mathcal{G}(R)$ with height $\Delta\mathcal{G}(R_{i*})$ we define the partial mass $m(R_{i*}) \equiv m_{i*}$ as

$$m_{i*}^2 \equiv \sqrt{\pi d R^2} \frac{\Delta\mathcal{G}(R_{i*}) \mathcal{G}(R_{i*})}{R_{i*}} \mu_J^2 \quad (3)$$

where we have used Eq. 2 to extract the (appropriately normalized) numerator of the angular structure function. Here

$$\mu_J^2 = \sum_{i \neq j} p_{Ti} p_{Tj} \Delta R_{ij}^2 \quad (4)$$

is the denominator of $\mathcal{G}(R)$ in Eq. 1 and is approximately equal to the squared jet mass m_J^2 . To see the physics that is encoded in the partial mass consider a jet with two infinitely narrow, hard subjets separated by an angular distance ΔR and with transverse momenta p_{T1} and p_{T2} . This jet will exhibit a single prominent peak in $\Delta\mathcal{G}(R)$ at $R = \Delta R$. The corresponding partial mass m_* will be given by $m_*^2 = p_{T1} p_{T2} \Delta R^2 \approx 2 p_1 \cdot p_2$.[¶] Thus the partial mass is a measure of the mass at a particular angular scale. For a jet whose substructure is determined by a heavy particle decay, the partial masses will be fixed by the kinematic constraints of the decay. This observation will be explored further in Sec. 3 in the context of top tagging.

Now that we have defined n_p , R_{i*} , and m_{i*} , we can ask how these jet observables characterize the substructure of a jet. First, for an idealized jet composed of n_s hard, narrow subjets with each pair of subjets separated by distinct angular scales R_{i*} , we expect the number of peaks n_p to be given by

$$n_p = n_p^{\max} \equiv \binom{n_s}{2} \quad (5)$$

In general this equality becomes an inequality $n_p \leq n_p^{\max}$ for jets whose substructure is less clean. For example, if some of the n_s subjets are wide or if some of the angular separations are approximately degenerate, then $\Delta\mathcal{G}(R)$ may exhibit fewer

[¶]Note that for two subjets j_1 and j_2 that are not infinitely narrow, the gaussian kernel in Eq. 2 introduces some amount of smearing in the partial mass.

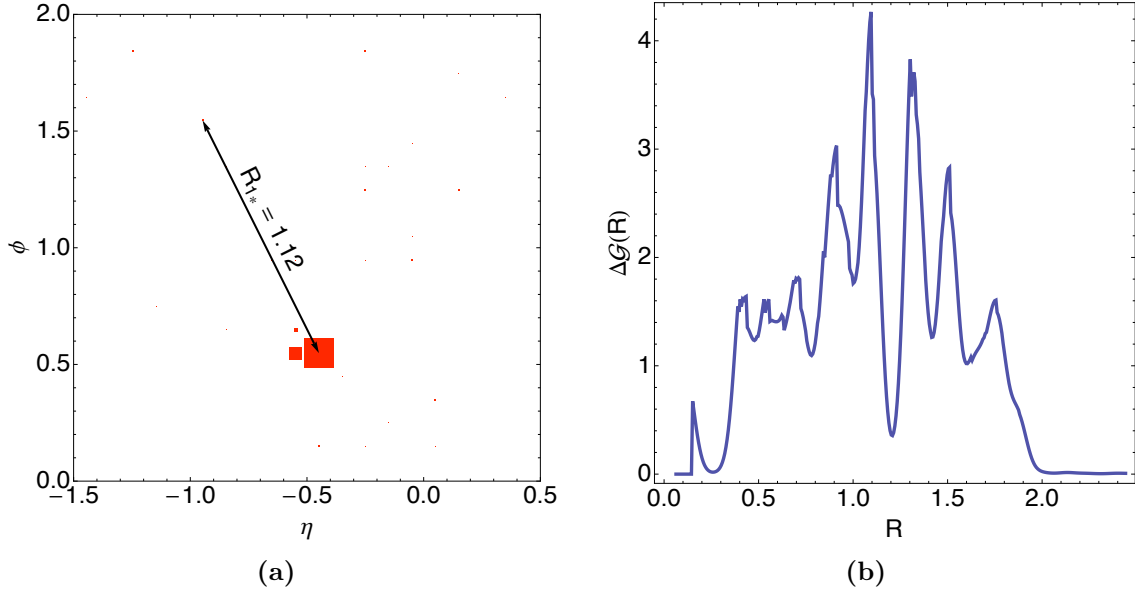


Figure 4: (a) p_T plot and (b) angular structure function $\Delta\mathcal{G}(R)$ for a QCD jet with diffuse substructure and $p_T \sim 600$ GeV. In the p_T plot, the small cell at the end of the arrow is so soft that it is barely visible. Prominent peaks in $\Delta\mathcal{G}(R)$ are distributed approximately uniformly in R . For a minimum prominence of 4.0, $\Delta\mathcal{G}(R)$ has a single peak at $R_{1*} = 1.09$. Note the scale of $\Delta\mathcal{G}(R)$ as compared to the top jet in Fig. 2(b).

than n_p^{\max} prominent peaks. When a prominent peak is resolvable, however, the resulting angular scale R_{i*} corresponds to an angular separation between two or more hard substructures in the jet. For a QCD jet, the distribution of prominent peaks should be roughly uniform in R , since QCD is approximately scale invariant. For a jet that is initiated by a heavy particle decay, the angular scales R_{i*} will be peaked at values characteristic of the decay kinematics of the heavy particle. The corresponding partial masses will be correlated to mass scales intrinsic to the heavy particle decay. In contrast, for QCD jets the partial masses will be peaked at small values, as determined by the soft and collinear singularities of QCD.

Some of the foregoing discussion is illustrated in Figs. 2 and 4. In Fig. 2 we show a boosted top jet with a clean three-pronged substructure. In the p_T plot in Fig. 2(a) the distances R_{i*} between the three hardest cells are indicated. From Fig. 2(b) we see that it is these same three angular scales that show up as prominent peaks in the angular structure function $\Delta\mathcal{G}(R)$. Less prominent peaks correspond to soft-hard correlations in the jet. The substructure of the QCD jet in Fig. 4(a) is quite different, with a single hard core surrounded by soft diffuse radiation. The mass of the jet is largely due to these soft, wide-angle emissions, and the most prominent peak in $\Delta\mathcal{G}(R)$ corresponds to correlations between the hard core of the jet and one such

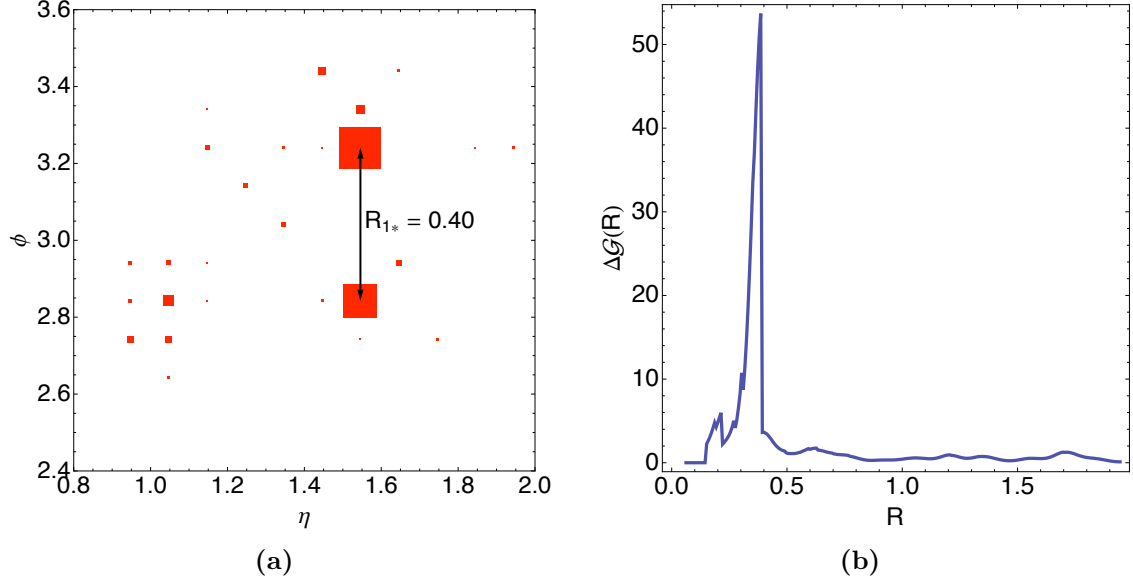


Figure 5: (a) p_T plot and (b) angular structure function $\Delta\mathcal{G}(R)$ for a top jet with $p_T \sim 500$ GeV. The decay products of the W^\pm are not individually resolved, with most of the radiation from the W^\pm ($\phi \sim 2.8$) contained within a single, hard cell. For a minimum prominence of 4.0, $\Delta\mathcal{G}(R)$ has a single peak at $R_{1*} = 0.39$.

emission. Prominent peaks in $\Delta\mathcal{G}(R)$ for this QCD jet are distributed approximately uniformly in R , as expected.

The close correspondence between structure in the p_T plots apparent by eye and the structure identified by the angular structure function $\Delta\mathcal{G}(R)$ is encouraging. To investigate the effectiveness of this procedure more thoroughly will require testing it against a concrete application, where the characteristics of the observables n_p , R_{i*} , and m_{i*} can be explored in greater detail. A good testbed will involve jets with complex substructure. For this reason we choose to construct a top tagging algorithm as a first application.

3 Top tagging

If every top jet had the clean three-pronged structure apparent in Fig. 2(a) then constructing an efficient top tagger would be straightforward. In practice, reconstruction of the top is complicated by a number of factors, including: (i) the finite resolution of the detector, which degrades mass and angular resolution; (ii) collinear radiation, which can make it difficult to resolve subjets initiated by hard partons that are close together; and (iii) the boost from the top rest frame to the lab frame,

which can result in decay products that are soft or overlap with one another. As a consequence, many top jets will have fewer than three prominent peaks in their angular structure functions. For example, in Fig. 5 we show an example of a top jet in which the W^\pm decay products do not exhibit a clean two-pronged structure. As a result $\Delta\mathcal{G}(R)$ only has a single prominent peak corresponding to mass correlations between the W^\pm and the b subjet. Constructing a tagger with high signal efficiencies will therefore require considering top jets with fewer than three prominent peaks in their angular structure functions.

This suggests that the following procedure could result in an efficient top tagging algorithm. Fix a minimum prominence h_0 . For each candidate jet, calculate the angular structure function and identify the number of peaks n_p with prominences exceeding h_0 . Reject candidate jets with $n_p = 0$ or $n_p > 3$ and sort the rest into bins with $n_p = 1, 2, 3$. Then apply separate sets of cuts to the R_{i*} and m_{i*} in each bin. This procedure has the advantage that candidate jets are being sorted with respect to their observed topologies. For example, top jets in which the decay products of the W^\pm are merged will be treated differently from top jets that exhibit a clean three-pronged substructure. In each bin cuts will be applied to the observables available from the identified substructure, and the cuts can be separately optimized to reflect the diversity of actual tops. By not requiring candidate jets to have the substructure of an idealized top jet with three distinct prongs, the top tagger can be more accommodating towards “ugly duckling” tops and thus attain higher signal efficiencies.

The outline of this section is as follows. In Sec. 3.1 we discuss distributions of the observables R_{i*} and m_{i*} for top jets and QCD jets. In Sec. 3.2 we present the details of our top tagging algorithm. In Sec. 3.3 we describe the Monte Carlo used to test the top tagger as well as the performance of the algorithm.

3.1 Observables

To set the stage for the top tagging algorithm defined in the next section, we first discuss what sort of top jet discrimination is available from the observables R_{i*} and m_{i*} . In Fig. 6 we illustrate distributions for these observables in the $n_p = 3$ bin. For top jets the kinematic constraints of the top decay in conjunction with the boost to the lab frame account for the basic features (see appendix A for details). Identifying the smallest R_* , i.e. R_{1*} , with the angle between the b subjet and the closer of the W^\pm subjets, we expect that $R_{1*} \sim 0.25$ for this $500 \text{ GeV} \leq p_T \leq 600 \text{ GeV}$ bin. Similarly, identifying R_{2*} with the angle between the two W^\pm subjets and R_{3*} with the angle between the b subjet and the further of the W^\pm subjets, we expect that $R_{2*} \sim 0.50$ and $R_{3*} \sim 0.75$. With these identifications for the three peaks, the predictions for the partial masses become $m_{1*} \sim 50 \text{ GeV}$, $m_{2*} \sim m_W$, and $m_{3*} \sim 140$

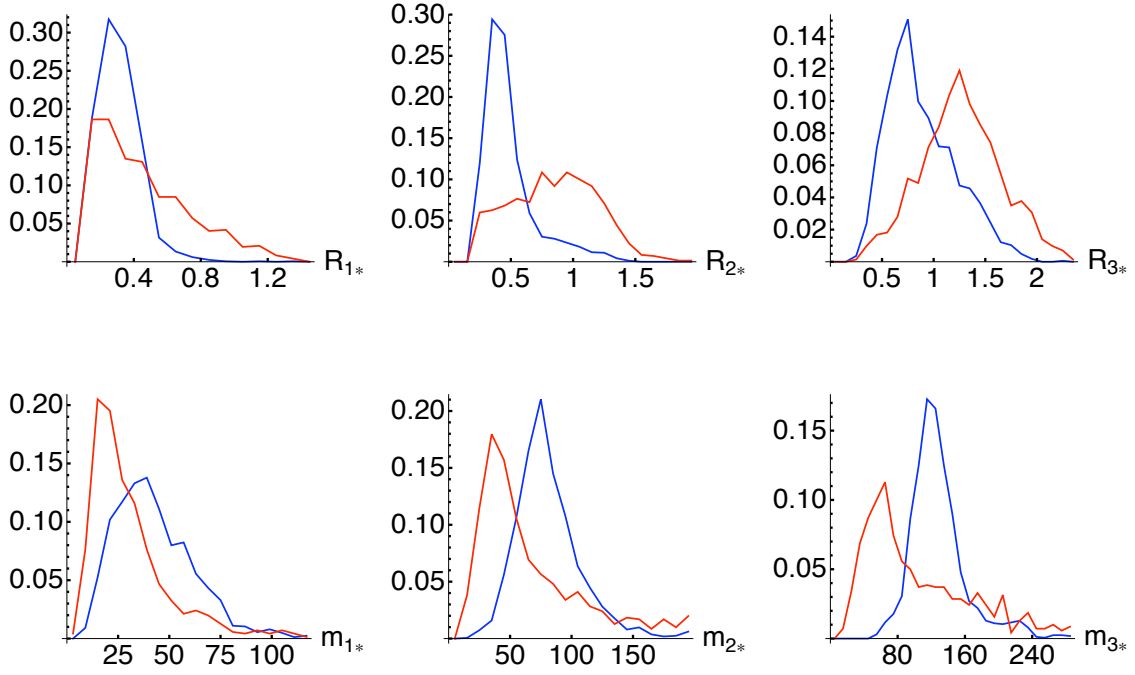


Figure 6: Distributions for observables in the $n_p = 3$ bin with $500 \text{ GeV} \leq p_T \leq 600 \text{ GeV}$. Distributions for top jets (QCD jets) are shown in blue (red). Angular scales R_{i*} and partial masses m_{i*} are ordered so that $R_{1*} \leq R_{2*} \leq R_{3*}$. For QCD the R_{i*} distributions are consistent with scale-invariant emission, while the m_{i*} distributions peak towards small partial masses. For tops the R_{i*} and m_{i*} distributions are peaked at angular and mass scales characteristic of top decay kinematics.

GeV. These predictions for the R_{i*} and m_{i*} match up well with the distributions in Fig. 6, although in practice the corresponding identifications only hold on the average. Note that the kinematic constraints of the top quark decay imply strong correlations between R_{i*} and m_{i*} for each i . This is illustrated in Fig. 7, where R_{2*} has been plotted against m_{2*} in the $n_p = 3$ bin. For QCD jets R_{2*} and m_{2*} are uncorrelated.

In contrast to top jets, QCD jets have no intrinsic scales. Since QCD is approximately scale invariant and the derivative in $\Delta\mathcal{G}(R)$ is with respect to $\log R$, we expect the R_* distributions to be approximately uniform. Imposing the ordering $R_{1*} \leq R_{2*} \leq R_{3*}$ then has the consequence that the R_{1*} distribution should peak at $R = 0$, the R_{2*} distribution should peak at intermediate R , and the R_{3*} distribution should peak towards large R . This is consistent with what is seen in Fig. 6, up to edge effects at large R in the R_{3*} distribution. The partial masses of QCD jets are peaked towards small m_{i*} , as we expect given that the physics of m_{i*} is qualitatively similar to the physics of jet masses m_J .

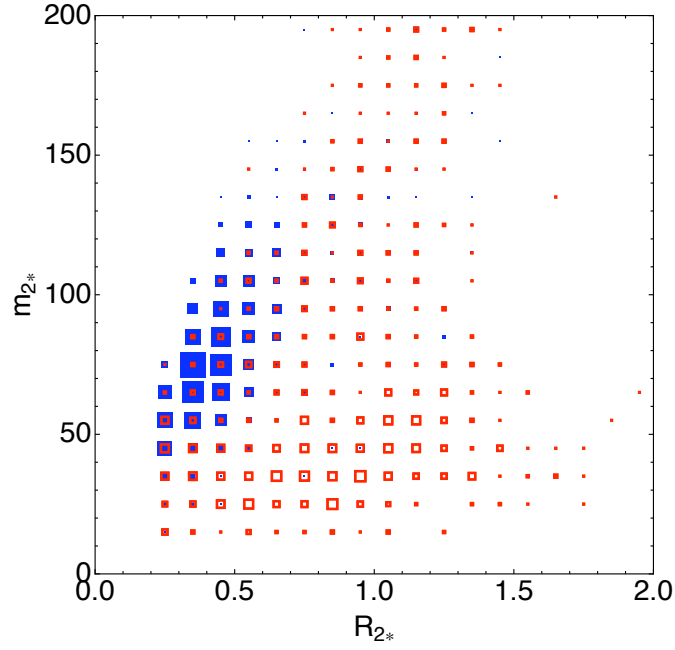


Figure 7: Correlations between R_{2*} and m_{2*} in the $n_p = 3$ bin with $500 \text{ GeV} \leq p_T \leq 600 \text{ GeV}$. For the top kinematic constraints imply strong correlations between R_{2*} and m_{2*} , while for QCD jets the two are uncorrelated. Correlations for top jets (QCD jets) are depicted in blue (red).

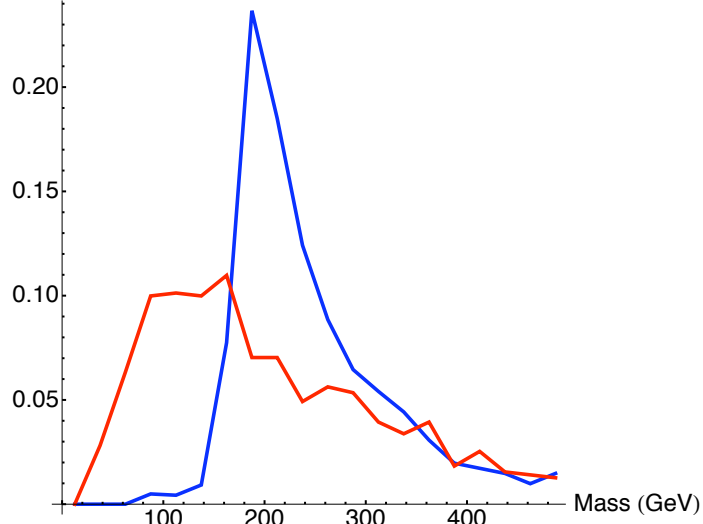


Figure 8: The jet mass m_J for tops (blue) and QCD (red) in the $n_p = 3$ bin with $500 \text{ GeV} \leq p_T \leq 600 \text{ GeV}$.

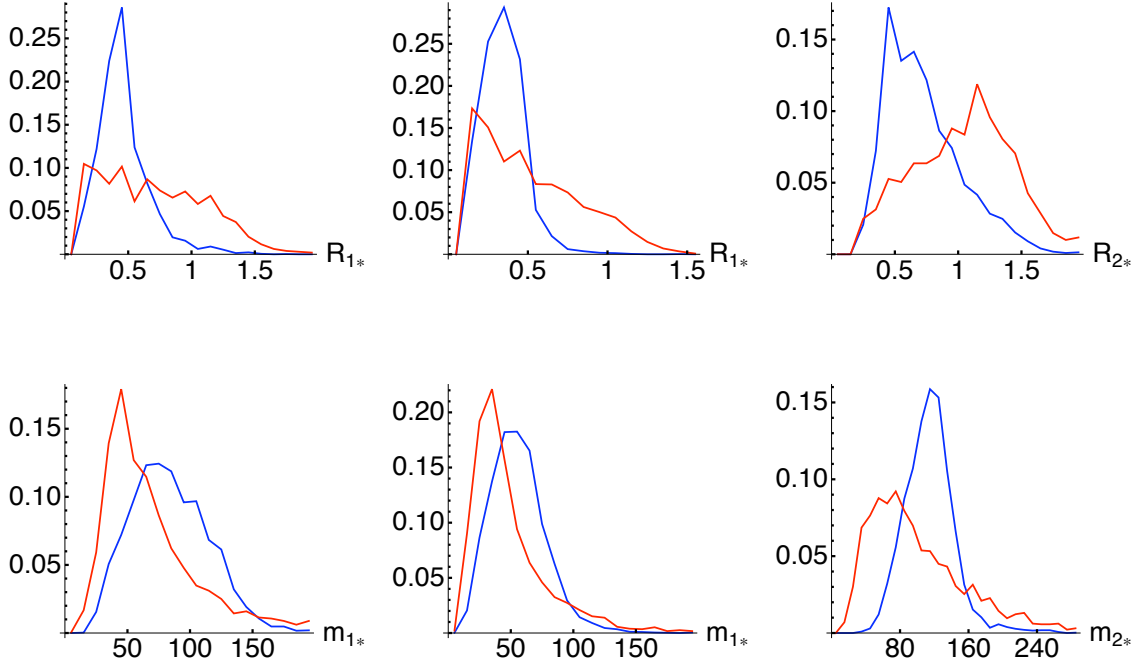


Figure 9: Distributions for R_{i*} and m_{i*} in the $n_p = 1, 2$ bins with $500 \text{ GeV} \leq p_T \leq 600 \text{ GeV}$. The leftmost column is $n_p = 1$, and the two rightmost columns are $n_p = 2$.

The features of the distributions in the $n_p = 1, 2$ bins are qualitatively similar, see Fig. 9. Here it is less clear what identifications to make for the different peaks, and it is likely that there is a fair amount of mixing between different decay topologies. In any case the observables derived from $\Delta\mathcal{G}(R)$ in the $n_p = 1, 2$ bins make effective discriminants between top jets and QCD jets, although more discrimination is available in the $n_p = 3$ bin. The distributions for R_{1*} and m_{1*} in the $n_p = 1$ bin are consistent with correlations between the W^\pm subjets j_{W1} and j_{W2} ; one possibility is that for these top jets the b subjet is too soft to yield prominent peaks. The distributions for the $n_p = 2$ bin are consistent with correlations between the b subjet and each of the two W^\pm subjets; one possibility is that for these top jets the W^\pm subjets j_{W1} and j_{W2} are nearly merged so that correlations between j_{W1} and j_{W2} do not result in any prominent peaks.

3.2 An algorithm

The distributions in Figs. 6-9 suggest that imposing cuts on m_J , R_{i*} , and m_{i*} could lead to effective discrimination between top jets and QCD jets. To test this we employ the following top tagging algorithm. Using the CA algorithm, cluster the event into fat jets with $R = 1.5$. Before applying any cuts, first presort the candidate

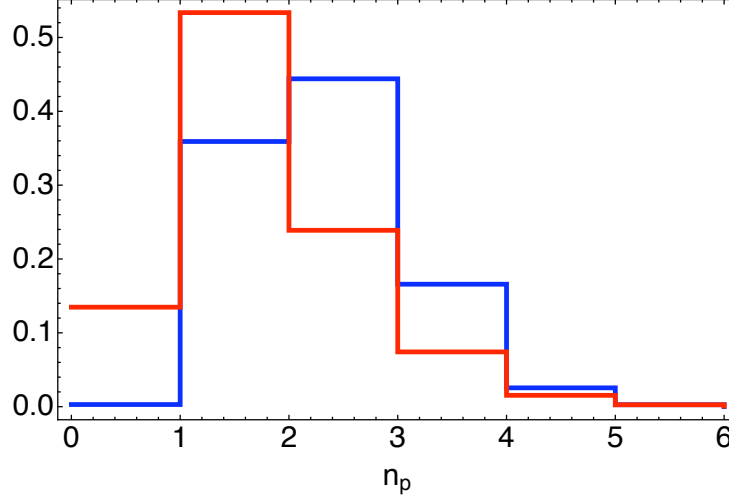


Figure 10: Fractions of top jets (blue) and QCD jets (red) that have n_p prominent peaks. Here the minimum prominence is $h_0 = 4.0$ and $500 \text{ GeV} \leq p_T \leq 600 \text{ GeV}$. These fractions exhibit only a small dependence on p_T .

jets into p_T bins of width 100 GeV. Then for each candidate jet calculate $\Delta\mathcal{G}(R)$ and identify the number of peaks n_p whose prominence exceeds a fixed minimum prominence $h_0 = 4.0$. This value of h_0 has been selected by scanning over a range $h_0 \in [1.0, 10.0]$ and choosing h_0 to minimize the background efficiency over a wide range of p_T and signal efficiencies. Within each p_T bin further sort the candidate jets into three peak bins ($n_p = 1, 2, 3$), throwing out jets with $n_p = 0$ or $n_p > 3$. This n_p cut removes a sizable fraction ($\sim 15\%$) of QCD jets, while rejecting only $\sim 3\%$ of top jets, see Fig. 10. For discrimination between top jets and QCD jets to be most effective one would like to disentangle the correlations between the observables as much as possible; for simplicity, however, we choose to make rectangular cuts in the space of observables. In particular, in the $n_p = 3$ bin we choose to impose cuts on six of the seven available observables, excluding m_{1*} , which is the least discriminating observable. More specifically, we impose the following cuts:

1. $m_J > m_{t \text{ min}}$
2. $R_{1*} < R_{1*}^{\text{max}}, R_{2*} < R_{2*}^{\text{max}}, R_{3*} < R_{3*}^{\text{max}}$
3. $m_{2*} > m_{2*}^{\text{min}}, m_{3*} > m_{3*}^{\text{min}}$

A candidate jet that passes this set of cuts is tagged as a top jet. In the $n_p = 1, 2$ bins we employ the corresponding set of cuts, except in contrast to the $n_p = 3$ bin, we make use of all of the observables. Also, we impose an additional cut $m_J < m_{t \text{ max}}$ in the $n_p = 1$ bin only, since the smaller number of observables in the $n_p = 1$ bin

(three) means that imposing this cut does not substantially increase the computer time needed to find optimal cuts. For the moment we leave the values of the cuts unspecified; this will be addressed in the next section.

3.3 Results

We use two different event samples for evaluating the performance of the top tagger. These event samples (from pp collisions with center of mass energy of 7 TeV) belong to a set of benchmark event samples that have been made publicly available by participants of the BOOST 2010 workshop [32]. The first event sample is generated by HERWIG 6.510 [33] with the underlying event simulated by JIMMY [34], which has been configured with a tune used by ATLAS. The second is generated by PYTHIA 6.4 [35] with Q^2 -ordering and the ‘DW’ tune for the underlying event. See [36] for more details. Unless noted otherwise, all results presented in this paper make use of the HERWIG event samples; the PYTHIA event samples were used as crosschecks. For signal jets we use the hardest jet in each event of a Standard Model hadronic $t\bar{t}$ sample, excluding jets with $|\eta| > 2.5$. For background jets we use the hardest jet in each event of a Standard Model dijet sample, again excluding jets with $|\eta| > 2.5$. For both event samples there are $\mathcal{O}(10^4)$ events in each p_T bin of width 100 GeV. For jet clustering we use the CA algorithm [17] with $R = 1.5$ as implemented by FastJet 2.4.2 [37]. In order to simulate the finite resolution of the ATLAS or CMS calorimeters, particles in each event are clustered into 0.1×0.1 cells in (η, ϕ) and then combined into massless four-vector pseudoparticles that are fed into FastJet. For each p_T window the cuts are chosen to yield the smallest background efficiency ϵ_B at each fixed signal efficiency ϵ_S . This optimization is performed by a custom Monte Carlo code that finely samples the space of cuts. Some sample values for the different cuts are given in Table 1.

In Fig. 11(a) and Fig. 11(b) we illustrate the performance of the top tagger. The performance is comparable to other top taggers in the literature [6–8, 27, 38–42], with $\epsilon_B \sim 5\%$ for $\epsilon_S = 50\%$ and $\epsilon_B \sim 0.5\%$ for $\epsilon_S = 20\%$ [36]. For a fixed signal efficiency, the background efficiency is approximately flat across the p_T range we have tested, $200 \text{ GeV} \leq p_T \leq 800 \text{ GeV}$. In Table 1 we see that in the $n_p = 2$ and especially $n_p = 3$ bins, where correspondingly more observables are available for discrimination, the top tagger is able to attain large signal efficiencies. Because the net signal and background efficiencies are obtained by combining all three n_p bins, the largest contribution to ϵ_S is actually from the $n_p = 2$ bin, since the plurality of top jets land in the $n_p = 2$ bin for $h_0 = 4.0$ (see Fig. 10). For example, at $\epsilon_S = 50\%$ and for $500 \text{ GeV} \leq p_T \leq 600 \text{ GeV}$ about 55% of tagged top jets come from the $n_p = 2$ bin, while about 20% and 25% come from the $n_p = 1$ and $n_p = 3$ bins, respectively. Similarly, the background efficiency is lowest in the $n_p = 1$ bin; only QCD jets with two or three prominent peaks do a good job of faking the substructure of a top jet. For example, at $\epsilon_S = 50\%$

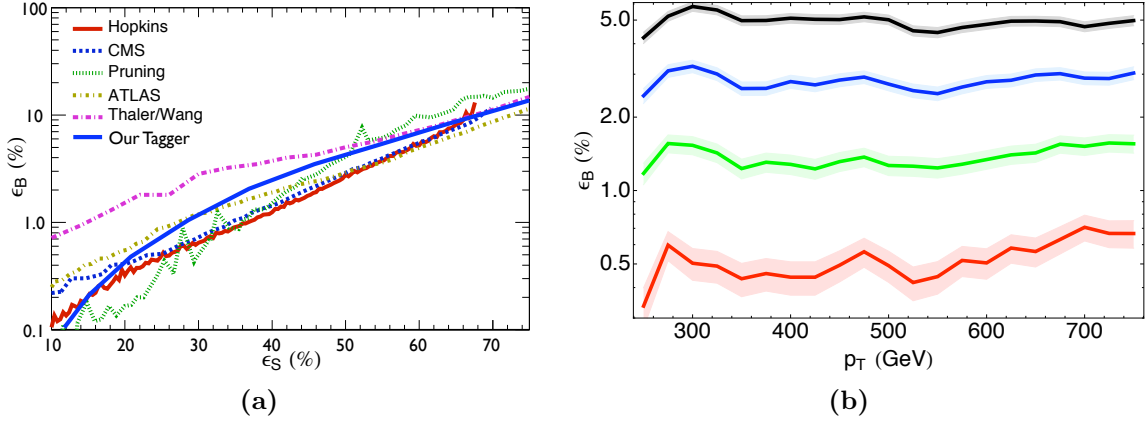


Figure 11: The performance of the top tagger as given by the **HERWIG** event samples. The background efficiency vs. signal efficiency for our top tagger is compared to other algorithms in the literature in (a). This figure is reproduced from [36] with the results from our tagger added. Here the candidate jets have transverse momenta $500 \text{ GeV} \leq p_T \leq 600 \text{ GeV}$. In (b) the background efficiency is plotted as a function of p_T for signal efficiencies of $\epsilon_S = 50\%$ (black), 40% (blue), 30% (green) and 20% (red). Efficiencies at a given p_{T0} are calculated from a p_T window of 100 GeV centered at p_{T0} . Note that, as a consequence, each point is not statistically independent. Error bands are statistical.

| $n_p = 1$ | $m_{t \text{ min}}$ | $m_{t \text{ max}}$ | R_{1*}^{max} | m_{1*}^{min} | $\epsilon_S(\%)$ | $\epsilon_B(\%)$ |
|---------------|---------------------|---------------------|-----------------------|-----------------------|------------------|------------------|
| 300 – 400 GeV | 177 GeV | 300 GeV | 0.96 | 78 GeV | 23.8 | 1.9 |
| 500 – 600 GeV | 175 GeV | 300 GeV | 0.57 | 74 GeV | 27.0 | 2.6 |

| $n_p = 2$ | $m_{t \text{ min}}$ | R_{1*}^{max} | R_{2*}^{max} | m_{1*}^{min} | m_{2*}^{min} | $\epsilon_S(\%)$ | $\epsilon_B(\%)$ |
|---------------|---------------------|-----------------------|-----------------------|-----------------------|-----------------------|------------------|------------------|
| 300 – 400 GeV | 157 GeV | 0.85 | 1.59 | 30 GeV | 77 GeV | 57.2 | 11.4 |
| 500 – 600 GeV | 159 GeV | 0.57 | 1.00 | 36 GeV | 55 GeV | 59.6 | 9.8 |

| $n_p = 3$ | $m_{t \text{ min}}$ | R_{1*}^{max} | R_{2*}^{max} | R_{3*}^{max} | m_{2*}^{min} | m_{3*}^{min} | $\epsilon_S(\%)$ | $\epsilon_B(\%)$ |
|---------------|---------------------|-----------------------|-----------------------|-----------------------|-----------------------|-----------------------|------------------|------------------|
| 300 – 400 GeV | 102 GeV | 0.81 | 1.03 | 2.11 | 26 GeV | 79 GeV | 82.9 | 15.9 |
| 500 – 600 GeV | 155 GeV | 0.62 | 0.66 | 1.35 | 46 GeV | 73 GeV | 73.6 | 7.9 |

Table 1: Sample optimized cut parameters at a (total) signal efficiency of $\epsilon_S = 50\%$ for two different p_T bins. In the rightmost column we show the signal and background efficiencies obtained within each n_p bin taken separately; i.e. these numbers do not take into account what fraction of candidate jets end up in each n_p bin. Signal efficiency increases substantially with n_p .

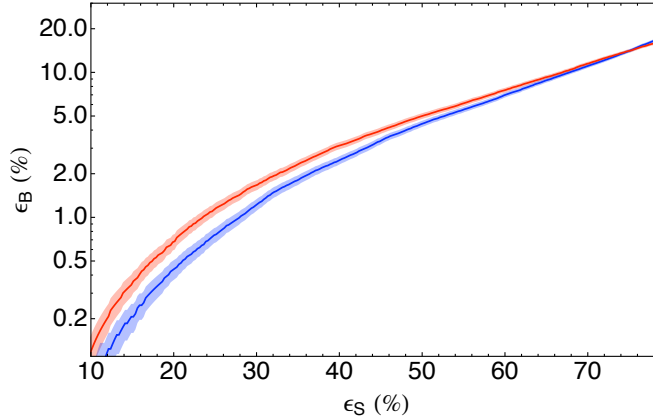


Figure 12: Signal versus background efficiency curves for **HERWIG** (blue) and **PYTHIA** (red) event samples in the $500 \text{ GeV} \leq p_T \leq 600 \text{ GeV}$ p_T bin. Error bands are statistical.

and for $500 \text{ GeV} \leq p_T \leq 600 \text{ GeV}$ about 32%, 54%, and 14% of tagged QCD jets come from the $n_p = 1$, $n_p = 2$, and $n_p = 3$ bins, respectively, even though only about 31% of QCD jets fall in the $n_p = 2$ or 3 bins.

As a crosscheck in Fig. 12 we compare the performance of the top tagging algorithm between the **HERWIG** and **PYTHIA** event samples. We see that the background efficiency is generally lower for **HERWIG** than it is for **PYTHIA**. One possible reason for this is that although the cut parameters have been separately optimized for both event generators, the parameters $h_0 = 4.0$ and $dR = 0.06$ were optimized on the basis of the **HERWIG** event samples. The **HERWIG** and **PYTHIA** event samples already disagree at the level of the n_p distributions, and this disagreement persists in the absence of the underlying event. This means that the typical prominence of peaks in $\Delta\mathcal{G}(\mathcal{R})$ differs between the two event samples. It would be interesting to understand in detail which features of the two event generators (the parton shower description, the underlying event model, etc.) contribute to this disagreement. Going further in this direction, however, lies outside the scope of this paper.

Given the large number of cut parameters that enter into the top tagging algorithm, overtraining is a concern. By training the cut parameters on a subset A of the event samples and testing the resulting cuts on subsets B_i disjoint from A , we can get some idea for how susceptible the quoted efficiencies are to overtraining. We find that the variation in the background efficiency ϵ_B (at fixed ϵ_S) that results from this validation procedure is comparable to the quoted statistical uncertainties. This additional uncertainty should be kept in mind when considering the absolute performance of the top tagger. Since precise estimates for background efficiencies are made difficult by other uncertainties, such as those which enter the modeling of QCD backgrounds or detector mock-up, we do not consider overtraining any further.

4 Discussion

By sorting jets according to the number of prominent peaks identified in their angular structure functions $\Delta\mathcal{G}(R)$ and making rectangular cuts on the angular and mass scales R_{i*} and m_{i*} , we have been able to construct an efficient top tagging algorithm. Since the focus of this paper has been to demonstrate that $\Delta\mathcal{G}(R)$ can be used to identify angular and mass scales in jets, the particular algorithm we have described was chosen for its simplicity. A number of possible improvements to the algorithm suggest themselves, however, even leaving aside modifications that are unrelated to the use of $\Delta\mathcal{G}(R)$. One possible concern is the large number of cut parameters that result from using three peak bins. Given the strong correlations between the R_{i*} and m_{i*} (see Fig. 7), one way to reduce the total number of free parameters would be to consolidate some of the variables. For example, one could replace separate cuts on R_{i*} and m_{i*} with a single cut on m_{i*}/R_{i*} . One could also investigate different schemes for binning identified peaks in $\Delta\mathcal{G}(R)$. For example, the expected substructure of a top might be better captured by sorting into bins $\{n_{p0}, n_{p1}\}$, where bin $\{n_{p0}, n_{p1}\}$ contains n_{p0} peaks with prominence $P \geq h_0$ and n_{p1} peaks with prominence $h_1 \leq P < h_0$. The definition of the partial mass in Eq. 3, which is most accurate for narrow subjets, could be improved to better capture the invariant mass of wide subjets. The particular way in which we organize the observables R_{i*} and m_{i*} according to their ordering in R as well as the use of topographic prominence to identify peaks could also be revisited. Since $\Delta\mathcal{G}(R)$ defines a continuous number of observables, this list of possible modifications could go on indefinitely, and it is interesting to ask whether our simple procedure makes efficient use of the information available from $\mathcal{G}(R)$. Going further in this direction, however, lies outside the scope of this paper.

Although we have explored the use of the angular correlation function $\mathcal{G}(R)$ and the angular structure function $\Delta\mathcal{G}(R)$ for the particular application of top tagging, the generality of the resulting procedure suggests that it could be useful in a variety of different contexts. It seems likely that procedures that make use of $\Delta\mathcal{G}(R)$ will be most effective when accurate reconstruction of angular scales is valuable. Some interesting possibilities include:

- using observables defined from $\Delta\mathcal{G}(R)$ to probe QCD; for example, measurements of R_* or n_p distributions for QCD jets could be compared against Monte Carlo calculations
- using R_* distributions to search for new physics (angular bumps instead of mass bumps); this is attractive, since accurate mass reconstruction is difficult
- calculating $\Delta\mathcal{G}(R)$ for the event as a whole and using the identified angular scales to determine an appropriate jet radius parameter R event-by-event

- using $\Delta\mathcal{G}(R)$ to access helicity/spin information in jetty cascades
- generalizing $\mathcal{G}(R)$ to some kind of n -particle correlation function, which might prove to be useful in the context of n -body decays
- using $\Delta\mathcal{G}(R)$ to zoom in on the prominent angular scales within a jet and defining some kind of ‘angular filtering’ procedure to improve mass resolution

By performing what is essentially an ‘angular fourier transform’ on the constituents of a jet, $\Delta\mathcal{G}(R)$ provides a convenient way of accessing angular and mass scales within jets. These angular and mass scales can be used to characterize the substructure of a jet. Further work will be needed to determine the extent to which the ideas explored in this paper can be applied more generally.

ACKNOWLEDGEMENTS

The authors thank Michael Peskin and Jay Wacker for useful discussions on jets and perturbative QCD. The authors would also like to thank JoAnne Hewett, Michael Peskin, and Jay Wacker for helpful feedback on the manuscript. A.L. thanks Steve Ellis, Matt Strassler and Jon Walsh for an introduction to jets and motivation for studying jet substructure when the field was still in its infancy. This work is supported by the US Department of Energy under contract DE-AC02-76SF00515. M.J. receives partial support from the Stanford Institute for Theoretical Physics and A.L. is also supported by an LHC Theory Initiative Travel Award.

A Top Quark Decay Kinematics

If we make some simplifying assumptions about the kinematics of top quark decays, then we can derive compact formulas for the angular scales R_{i*} where we expect top jets to have significant substructure. To do so we first work in the approximation that both the top and the W^\pm decay isotropically in their rest frames. Then working in the limit of large transverse momenta, we can approximate the typical momentum fractions of the decay products of the top in the lab frame as

$$z_{W1} = z_{W2} = \frac{1}{2}z_W = \frac{m_t^2 + m_W^2}{4m_t^2} \simeq 0.30 \quad z_b = \frac{m_t^2 - m_W^2}{2m_t^2} \simeq 0.40 \quad (6)$$

A typical configuration [43] has the decay products approximately distributed along a line with

$$R_{b1} \leq R_{12} \leq R_{b2} \quad (7)$$

Assuming that the decay topology is exactly line-like with

$$R_{b2} = R_{12} + R_{b1} \quad (8)$$

we can use mass constraints to determine the R_{i*} and m_{i*}

| | $i = 1$ | $i = 2$ | $i = 3$ |
|------------|---|---|---|
| R_{i*} | $\frac{2m_t^2}{p_T} \frac{m_t - m_W}{m_t^2 + m_W^2}$ | $\frac{2m_t^2}{p_T} \frac{2m_w}{m_t^2 + m_W^2}$ | $\frac{2m_t^2}{p_T} \frac{m_t + m_W}{m_t^2 + m_W^2}$ |
| m_{i*}^2 | $\frac{(m_t - m_W)^2}{2} \frac{m_t^2 - m_W^2}{m_t^2 + m_W^2}$ | m_W^2 | $\frac{(m_t + m_W)^2}{2} \frac{m_t^2 - m_W^2}{m_t^2 + m_W^2}$ |

where p_T is the transverse momentum of the top quark. Numerical values of these expressions for $p_T = 550$ GeV are given in Sec. 3.2.

References

- [1] M. H. Seymour, Z. Phys. **C62**, 127-138 (1994).
- [2] J. M. Butterworth, B. E. Cox, J. R. Forshaw, Phys. Rev. **D65**, 096014 (2002).
[arXiv:hep-ph/0201098].
- [3] A. Katz, M. Son, B. Tweedie, [arXiv:1010.5253].
- [4] Y. Cui, Z. Han, M. D. Schwartz, [arXiv:1012.2077].
- [5] L. G. Almeida, S. J. Lee, G. Perez *et al.*, Phys. Rev. **D79**, 074012 (2009).
[arXiv:0810.0934].
- [6] J. Thaler, L. -T. Wang, JHEP **0807**, 092 (2008). [arXiv:0806.0023].
- [7] G. Brooijmans, **ATLAS** note, **ATL-PHYS-CONF-2008-008**.
- [8] D. E. Kaplan, K. Rehermann, M. D. Schwartz *et al.*, Phys. Rev. Lett. **101**, 142001 (2008). [arXiv:0806.0848].
- [9] T. Plehn, G. P. Salam, M. Spannowsky, Phys. Rev. Lett. **104**, 111801 (2010).
[arXiv:0910.5472].
- [10] T. Plehn, M. Spannowsky, M. Takeuchi *et al.*, JHEP **1010**, 078 (2010).
[arXiv:1006.2833].

- [11] J. M. Butterworth, A. R. Davison, M. Rubin *et al.*, Phys. Rev. Lett. **100**, 242001 (2008). [arXiv:0802.2470]; AIP Conf. Proc. **1078**, 189-191 (2009). [arXiv:0809.2530].
- [12] G. D. Kribs, A. Martin, T. S. Roy, M. Spannowsky, Phys. Rev. **D81**, 111501 (2010). [arXiv:0912.4731]; Phys. Rev. **D82**, 095012 (2010). [arXiv:1006.1656].
- [13] J. -H. Kim, [arXiv:1011.1493].
- [14] C. -R. Chen, M. M. Nojiri, W. Sreethawong, JHEP **1011**, 012 (2010). [arXiv:1006.1151].
- [15] A. Falkowski, D. Krohn, L. -T. Wang, J. Shelton, A. Thalapillil, [arXiv:1006.1650].
- [16] C. Hackstein and M. Spannowsky, Phys. Rev. D **82**, 113012 (2010) [arXiv:1008.2202].
- [17] Y. L. Dokshitzer, G. D. Leder, S. Moretti, B. R. Webber, JHEP **9708**, 001 (1997). [arXiv:hep-ph/9707323]; M. Wobisch, T. Wengler, [arXiv:hep-ph/9907280]; M. Wobisch, DESY-THESIS-2000-049.
- [18] S. Catani, Y. L. Dokshitzer, M. H. Seymour *et al.*, Nucl. Phys. **B406**, 187-224 (1993); S. D. Ellis, D. E. Soper, Phys. Rev. **D48**, 3160-3166 (1993). [arXiv:hep-ph/9305266].
- [19] L. G. Almeida, S. J. Lee, G. Perez *et al.*, Phys. Rev. **D82**, 054034 (2010). [arXiv:1006.2035].
- [20] J. Thaler and K. Van Tilburg, [arXiv:1011.2268].
- [21] L. G. Almeida, S. J. Lee, G. Perez, G. F. Sterman, I. Sung, J. Virzi, Phys. Rev. **D79**, 074017 (2009). [arXiv:0807.0234].
- [22] J. Gallicchio, M. D. Schwartz, Phys. Rev. Lett. **105**, 022001 (2010). [arXiv:1001.5027].
- [23] A. Hook, M. Jankowiak, J. G. Wacker, [arXiv:1102.1012].
- [24] D. E. Soper and M. Spannowsky, [arXiv:1102.3480].
- [25] K. Black, J. Gallicchio, J. Huth *et al.*, [arXiv:1010.3698].
- [26] R. Alon, E. Duchovni, G. Perez, A. P. Pranko and P. K. Sinervo, [arXiv:1101.3002].

- [27] S. D. Ellis, C. K. Vermilion, J. R. Walsh, Phys. Rev. **D81**, 094023 (2010). [[arXiv:0912.0033](#)].
- [28] F. Abe *et al.* [CDF Collaboration], Phys. Rev. Lett. **70**, 713-717 (1993).
- [29] S. D. Ellis, Z. Kunszt, D. E. Soper, Phys. Rev. Lett. **69**, 3615-3618 (1992). [[hep-ph/9208249](#)].
- [30] A. Bialas, R. B. Peschanski, Nucl. Phys. **B273**, 703 (1986).
- [31] A discussion of prominence as well as lists of prominent peaks throughout the world can be found at: A. Maizlish, [www.peaklist.org](#).
- [32] Events are located at:
<http://www.lpthe.jussieu.fr/~salam/projects/boost2010-events/>
<http://tev4.phys.washington.edu/TeraScale/boost2010/>
- [33] G. Corcella, I. G. Knowles, G. Marchesini *et al.*, [[arXiv:hep-ph/0210213](#)].
- [34] J. M. Butterworth, J. R. Forshaw, M. H. Seymour, Z. Phys. **C72**, 637-646 (1996). [[arXiv:hep-ph/9601371](#)].
- [35] T. Sjostrand, S. Mrenna, P. Z. Skands, JHEP **0605**, 026 (2006). [[arXiv:hep-ph/0603175](#)].
- [36] A. Abdesselam, E. B. Kuutmann, U. Bitenc *et al.*, [[arXiv:1012.5412](#)].
- [37] M. Cacciari, G. P. Salam, Phys. Lett. **B641**, 57-61 (2006). [[arXiv:hep-ph/0512210](#)].
- [38] **CMS** Collaboration, R. Adolphi *et al.*, *A Cambridge-Aachen (C-A) based jet algorithm for boosted top jet tagging, CMS Physics Analysis Summary*
- [39] **CMS** Collaboration, R. Adolphi *et al.*, CMS Physics Analysis Summary **CMS-PAS-EXO-09-002** (2009).
- [40] S. Rappoccio, CMS CR-2009/255. Geneva, March, 2010.
- [41] **ATLAS** Collaboration, **ATL-PHYS-PUB-2009-081**.
- [42] **ATLAS** Collaboration, Tech. Rep. **ATL-PHYS-PUB-2010-008**, CERN, Geneva, Jul, 2010.
- [43] M. Fischer, S. Groote, J. G. Korner, M. C. Mauser, Phys. Rev. **D65**, 054036 (2002). [[arXiv:hep-ph/0101322](#)].